Collisional excitation kinetics for math xmlns="http://www.w3.org/1998/Math/MathML">mrow>mi mathvariant="normal">O/mi>mo>(/mo>mn>3/mn>mi>s/mi>mspace width="0.16em">/mspace> mmultiscripts>mi>S/mi>none>/none>mi>o/mi>mprescripts>/mprescripts>none>/none>mn>5/mn>/mmultiscripts>mo>)/mo>/mrow>/math> and math xmlns="http://www.w3.org/1998/Math/MathML">mrow>mi mathvariant="normal">O/mi>mo>(/mo>mn>3/mn>mi>p/mi>mspace width="0.16em">/mspace> mmultiscripts>mi>P/mi>mn>3/mn>none>/none>mprescripts>/mprescripts>none>/none>mn>5/mn>/mmultiscripts>mo>)/mo>/mrow>/math> states using laser absorption spectroscopy in shock-heated weakly ionized math xmlns="http://www.w3.org/1998/Math/MathML">msub>mi mathvariant="normal">O/mi>mn>2/mn>/msub>/math>-Ar mixture

Yang Li, Yu Wang, David F. Davidson, and Ronald K. Hanson

Phys. Rev. E **103**, 063211 — Published 21 June 2021

DOI: 10.1103/PhysRevE.103.063211

Collisional Excitation Kinetics of O(3s $^5S^o$) and O(3p $^5P_3$) States using Laser Absorption Spectroscopy in Shock-Heated Weakly-Ionized O_2-Ar Mixture

Yang Li,* Yu Wang, David F. Davidson, and Ronald K. Hanson

Department of Mechanical Engineering, Stanford University

(Dated: May 27, 2021)

Abstract

Collisional excitation kinetics for atomic oxygen is studied behind reflected shock waves in 1% O_2/Ar mixtures over 10,000 - 11,000 K using laser absorption spectroscopy of the O(3s $^5S^o$) to O(3p $^5P_3$) transition at 777 nm and the O(3p $^5P_3$) to O(3d $^5D^0_{2,3,4}$) transitions at 926 nm. Four time-histories are inferred simultaneously from the absorbance of the two transitions: the population density of level 4 of atomic oxygen, i.e. the O(3s $^5S^o$) state, n_4; the population density of level 6 of atomic oxygen, i.e. the O(3p $^5P_3$) state, n_6; the electron number density, n_e; and the heavy-particle translational temperature, T_{tr}. Atomic oxygen in the levels 4 and 6 are not in equilibrium with the ground state atomic oxygen as the measurements of n_4 and n_6 are generally 3-20 times smaller than the corresponding values under Boltzmann equilibrium at T_{tr}. However, these two states are close to partial equilibrium with each other within the test time, indicating strong heavy-particle cross coupling between levels 4 and 6 of atomic oxygen. A simplified two-temperature collisional-radiative (CR) model is developed to study the thermal and chemical non-equilibrium of atomic oxygen following shock heating. The four measured time-histories are used to optimize the twelve collisional rate constants in the CR model using a stochastic gradient descent (SGD) algorithm. The time-history results, diagnostic methods and collisional-radiative model presented in the current study are potentially useful in studies of high-enthalpy air, plasma processing or other applications involving weakly ionized oxygen.

NOMENCLATURE

Atomic Oxygen Level 1: O($2p^4$ ^{3}P), ground state atomic oxygen

Atomic Oxygen Level 4: O(3s $^5S^o$), probed by 777 nm transition absorption spectroscopy

* yli28@stanford.edu

Atomic Oxygen Level 6: O($3p\ ^5P_3$), probed by 926 nm transition absorption spectroscopy

Atomic Oxygen Level 10: O($3d\ ^5D^0_{2,3,4}$)

Cross-sectional slope constant: $\beta_{14}, \beta_{16}, \beta_{46}$, corresponding to the collisional excitation cross section of transition from atomic oxygen in the level 1 to 4, 1 to 6, and 4 to 6 in unit of cm^2/eV

I. INTRODUCTION

Under typical atmospheric re-entry conditions of a spacecraft, a bow shock forms ahead of the vehicle because of its high velocity[1–3]. The temperature immediately after the bow shock can be higher than 10,000K[4, 5]. At such high temperatures, molecular oxygen and nitrogen dissociate almost completely and produce atomic species in excited energy states and charged particles[6–8]. Radiation from the excited states can account for a significant portion of the total heat flux to the re-entry vehicle[1, 5, 9]. This radiation is heavily dependent on the population of the excited-state species, which are generally not in chemical and thermal equilibrium. Understanding the collisional excitation/ionization kinetics for atomic species is thus of crucial importance in predicting the evolution of the population of the excited-state species and thus the radiative heat flux for high-enthalpy air during re-entry missions[7].

In local thermal equilibrium (LTE), the populations of atomic oxygen in various electronic energy states follow the Boltzmann distribution characterized by a single temperature T[10]. Under large spatial or temporal gradients, however, the collisions among particles may not be sufficient to maintain such equilibrium[11]. Some multi-temperature kinetic models[9] assume that the excited-state species are in a Boltzmann distribution within each internal mode, and therefore are characterized by

electron translational temperature T_e, heavy particle translational temperature T_{tr}, electronic temperature T_{el}, vibrational temperature T_{vib}, and rotational temperature T_{rot}, respectively. More generally, a state-to-state collisional-radiative model can be used to study the kinetic behavior of the excited-state species individually[1, 8, 12–14]. Most of the previous kinetic models focus on the electron impact collisions because of the higher efficiency of electrons in exciting and ionizing molecules[1, 6, 7, 12]. However, heavy-particle-impact collisional excitation reactions (e.g., Ar + O(g) = Ar + O(3s ^{5}S^o)) can be important to the kinetics of high-enthalpy gases[2, 8, 15, 16], especially immediately behind the shock, where electrons are being produced from ionization processes but the number density is still low.

Bultel et al.[2], Lemal et al.[8] and Jo et al.[16] included the heavy-particle excitation rate constants in their state-to-state collisional-radiative models. Nations et al.[15] determined the heavy-particle excitation rate of the O(3s ^{5}S^o) state from its population time-history measurements using a 777 nm laser over 5,000-7,000K. Their measurements showed that the population of the O(3s ^{5}S^o) state remained 3 to 5 times smaller than the equilibrium value calculated from the Boltzmann distribution, during their experiment.

Li et al.[17] extended the measurements of the O(3s ^{5}S^o) population time-history and the heavy-particle reaction rate to 8,000-10,000K. These authors observed that the O(3s ^{5}S^o) population time-history had three stages within the 1 ms test time after the passage of the reflected shock wave. To explain this behavior, a two-temperature collisional-radiative model was developed, recognizing that electrons are not in thermal and chemical equilibrium within the test time. This model takes the initial temperature, pressure and mole fractions after the reflected shock as inputs, solves two energy conservation equations and five species conservation equations and outputs the time-histories of the translational temperature, O(3s ^{5}S^o) population, electron number density and populations of ground state argon, ground state atomic oxygen, Ar^+, and O^+. Electron number density and the heavy particle translational tempera-

ture are particularly important to the collisional excitation kinetics of atomic oxygen because of the higher excitation efficiency of electrons compared with heavy particles and the exponential dependence of the excitation rate constants on the translational temperature. Direct measurements of the electron number density and the translational temperature are thus needed to validate and improve the kinetic model.

To improve and extend the previous two-temperature collisional-radiative model for atomic oxygen[17], four time-histories, i.e. for the O(3s ^{5}S^o) population n_4, the O(3p ^{5}P$_3$) population n_6, the electron number density n_e and the translational temperature $T_{\rm tr}$, are simultaneously inferred using two lasers at 777 and 926 nm targeting the O(3s ^{5}S^o) to O(3p ^{5}P$_3$) and the O(3p ^{5}P$_3$) to O(3d ^{5}D$^0_{2,3,4}$) transitions from 10,000 to 11,000 K in the current study. The reaction rate constants of the kinetic model are optimized by minimizing the residual sum of squares between the model outputs and the measured time-histories.

The goals of this study are: (1) to extend the diagnostic methods for atomic oxygen to include the n_4, n_6, n_e, and $T_{\rm tr}$ time-histories and to extend the measurement temperature range to 10,000 - 11,000K (2) to study the thermal and chemical non-equilibrium behavior of the excited states of atomic oxygen over 10,000-11,000K, and (3) to utilize the measured time-histories to optimize the rate constants of the two-temperature collisional-radiative model for Ar-O_2 mixtures over 10,000-11,000K.

II. EXPERIMENTAL RESULTS

A. Experimental set-up

The schematic of the current experiment is presented in a previous paper[18] and repeated here in Figure 1. The shock tube and laser absorption spectroscopy probing the O(3s ^{5}S^o) to O(3p ^{5}P$_3$) transition are described in detail in previous papers[17, 18] and summarized below.

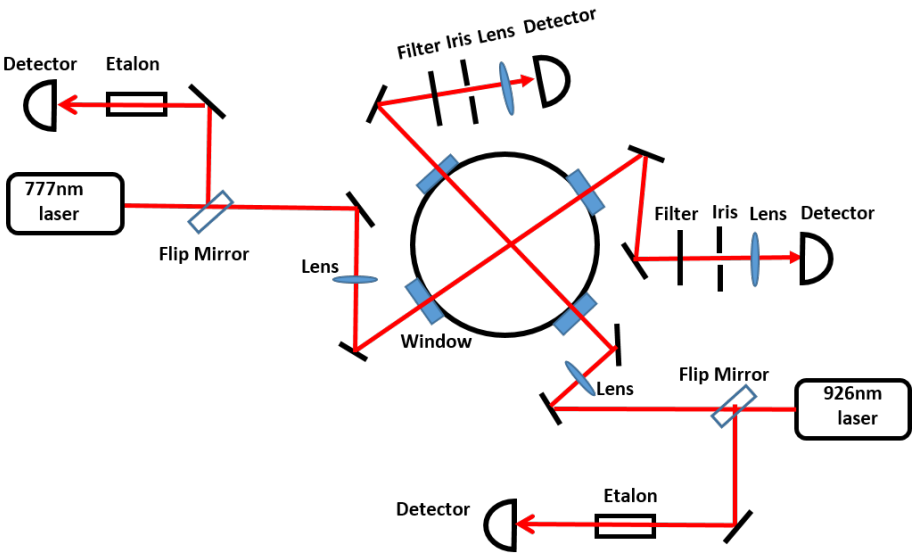

FIG. 1: Optical setup for absorbance measurements of the 777 and 926 nm transitions.

In a typical shock tube experiment in this study, the driven section of the shock tube was filled with 1% O_2/Ar (Praxair) to 0.7-1 torr. Then the driver section was filled with He (Praxair) to approximately 130-160 psia until the diaphragm separating the equal-area driver and driven sections ruptured. An incident shock was formed and traveled down the driven section. It was reflected off the endwall and the stagnant gas behind the reflected shock was heated to initial temperatures over 10,000 K. The velocity of the incident shock was measured using five piezoelectric pressure transducers and extrapolated to infer the velocity at the endwall. The temperature and pressure immediately behind the reflected shock were calculated using an in-house code named Frozen-chemistry shock calculator (FROSH), under the assumptions of no oxygen dissociation but vibrational and rotational equilibrium. The typical initial post-shock thermodynamic condition was 10,100-11,200 K and 0.3-0.5 atm. The typical duration of approximately constant pressure, i.e. the test time, was 500-600 μs, which was terminated by arrival of the reflection of the reflected shock from the

contact surface of the driver and driven gas. The light beam of a 777.2 nm laser Nanoplus targeting the O(3s ^{5}S^o) to O(3p ^{5}P$_3$) transition was propagated through a pair of wedged UV fused silica windows located 5 mm from the endwall. The light beam of a 926 nm laser Nanoplus, targeting the O(3p ^{5}P$_3$) to O(^{5}D$^0_{2,3,4}$) transition was propagated through another pair of wedged UV fused silica windows at the same axial location. Both of the lasers were modulated by 25kHz triangle waves. Etalons with free spectral range (FSR) of 0.0688 cm^{-1} were used to convert the laser light from the time domain to the frequency domain. The transmitted light intensities were measured by photodiode detectors (Thorlabs PDA36A, $f_{-3dB} \geq 1.6$MHz) and recorded at a sampling rate of 100 MS/s.

B. Spectroscopic theory

The absorbance α_ν at laser frequency ν is determined from the incident and transmitted light intensities by

$$\alpha_\nu = -\ln\left(\frac{I_t}{I_0}\right) = S_{lu} n_l L \phi(\nu) \tag{1}$$

where I_t and I_0 are the transmitted and incident light intensity, respectively; n_l is the number density of atomic oxygen in the the probed state O(3s ^{5}S^o) or O(3p ^{5}P$_3$); $L = 15.24$ cm is the optical path length; $\phi(\nu)$ is the lineshape function of the absorbance, which satisfies $\int_0^\infty \phi(\nu) d\nu = 1$ and ν is in cm^{-1}; S_{lu} is the line-strength of the transition and is given by

$$S_{lu}[\text{cm/molec}] = \frac{c}{8\pi\nu_0^2} A_{ul} \frac{g_u}{g_l} \left[1 - \exp\left(-\frac{h\nu_0}{k_B T}\right)\right] \tag{2}$$

where c is speed of light in cm/s, ν_0 is the transition frequency in Hz, A_{ul} is the Einstein coefficient of the transition in s^{-1}, and g_u and g_l are the degeneracies of the upper and lower states as summarized in Table I. Because the line-strength (S_{lu}) is only weakly dependent on temperature (T), the translational temperature inferred before O_2 dissociation is used in the above equation for simplicity.

TABLE I: Spectroscopic parameters for atomic oxygen transitions. E_l and E_u are the energy in wavenumber of the lower and upper states l and u. A_{ul} is the Einstein coefficient of the transition from u and l. g_l and g_u are the degeneracies of the l and u states.

Transition	Ritz Wavelength in Air (nm)	A_{ul} (s^{-1})	E_l (cm^{-1})	E_u (cm^{-1})	g_l	g_u
3s ^{5}S - 3p $^5P_3$	777.194	3.69×10^7	73768.200	86631.454	5	7
3p $^5P_3$ - 3d $^5D_2$	926.5826	2.97×10^6	86631.454	97420.839	7	5
3p $^5P_3$ - 3d $^5D_3$	926.5932	1.48×10^7	86631.454	97420.716	7	7
3p $^5P_3$ - 3d $^5D_4$	926.6006	4.45×10^7	86631.454	97420.630	7	9

The lineshape of the absorbance is determined by various broadening and shift mechanisms, including natural broadening, Doppler broadening and shift, resonance broadening, van der Waals broadening and shift, and Stark broadening and shift[19]. Natural broadening is usually three orders of magnitude smaller than the Doppler broadening and hence is neglected in the current study. Resonance broadening is also small and neglected because there is no allowed transition coupling the O(3s $^5S^o$) and O(3p $^5P_3$) states to the ground state.

Doppler broadening is the most significant broadening mechanism for the 777 and 926 nm transitions within the current temperature range of 10,000 to 11,000 K, as shown in figure 2. In the current study, the Doppler full-width at half-maximum (FWHM) of the 777 nm absorbance is used to infer the translational temperature of the gas because of its better signal-to-noise ratio (SNR). For gas with a Maxwellian velocity distribution, the Doppler broadening lineshape is a Gaussian function characterized by its FWHM, $\Delta\nu_D$. $\Delta\nu_D$ is given by[20]

$$\Delta\nu_D = \nu_0 \left(\frac{8kT\ln 2}{mc^2}\right)^{\frac{1}{2}} = 7.16 \times 10^{-7}\nu_0 \left(\frac{T}{M_O}\right)^{\frac{1}{2}} \tag{3}$$

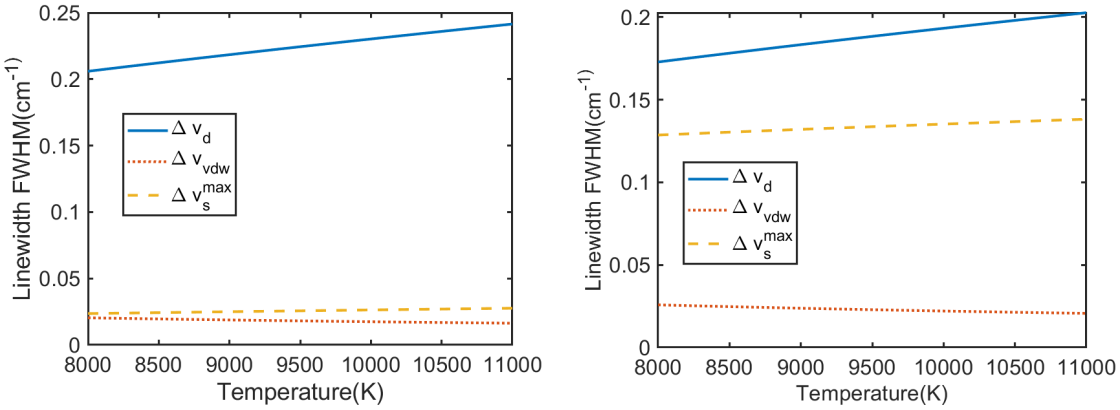

(a) (b)

FIG. 2: Comparison of Doppler broadening Δv_d, van der Waals broadening Δv_{vdw} and Stark broadening Δv_s^{max} at 0.5 atm for (a) the 777 nm transition and (b) the 926 nm transition. The Stark broadening Δv_s^{max} is calculated using the maximum n_e of the measurements, $n_e = 2.5 \times 10^{21}$ m^{-3}.

where k is the Boltzmann constant, m is the mass in kg, c is the speed of light, ν_0 is the transition line-center frequency in cm^{-1}, T is the translational temperature in K, M_O is the molecular weight of atomic oxygen. For temperatures from 8,000 to 11,000K, $\Delta\nu_D$ ranges from 0.21 to 0.25 cm^{-1}. The Doppler shift is neglected because the gas behind the reflected shock is generally considered to be stagnant.

The Stark broadening and shift are caused by collisions between the absorber and other charged particles. The FWHM of Stark broadening (in $\mathring{A}$) is given by[21–23].

$$\Delta\lambda_{Stark} \approx 2\left[1 + 1.75 \times 10^{-4} n_e^{\frac{1}{4}} \alpha \left(1 - 0.068 n_e^{\frac{1}{6}} T_e^{-\frac{1}{2}}\right)\right] 10^{-16} w n_e \tag{4}$$

and the shift(in $\mathring{A}$)

$$\delta\lambda_{Stark} \approx \left[\left(\frac{d}{w}\right) \pm 2.0 \times 10^{-4} n_e^{\frac{1}{4}} \alpha \left(1 - 0.068 n_e^{\frac{1}{6}} T_e^{-\frac{1}{2}}\right)\right] 10^{-16} w n_e \tag{5}$$

where T_e is the electron translational temperature, n_e is the electron number density, w is the electron impact half width, d/w is the relative electron-impact shift, and α is

the ion-broadening parameter. The values of w, d, α for the atomic oxygen transitions in this study can be found in Griem's book [23]. The electron number density is inferred from the Stark shift of the 926 nm transition using Equation 5. The large magnitude of the 926 nm Stark shift makes it sensitive to n_e and robust to noise.

The van der Waals broadening and shift are caused by the collisions of the absorber with charge neutral particles. Theoretical predictions of the van der Waals broadening and shift have large uncertainties in general.

The van der Waals broadening and the Stark broadening have Lorentzian lineshapes, characterized by their FWHMs $\Delta\nu_{vdw}$ and $\Delta\nu_s$. The total collisional broadening FWHM, $\Delta\nu_c$, is simply the summation of the two FWHMs.

Comparisons of Doppler broadening $\Delta\nu_d$, van der Waals broadening $\Delta\nu_{vdw}$, and Stark broadening $\Delta\nu_s$ width at $P = 0.5$ atm are shown in Figure 2 for the 777 and 926 nm transitions. The electron number density used to calculate $\Delta\nu_s$ in figure 2 is 2.5×10^{21} m^{-3}, which is the maximum electron number density at $T_{5,0}$ =11,200 K inferred from the Stark shift of the 926 nm transition in the current experiment. It is of note that according to the current measurements and model predictions, the electron number density does not reach the value corresponding to chemical equilibrium and the translational temperature drops continuously due to Ar ionization within the test time (around 500 μs). The combined effect of these two makes the Stark broadening almost 10 times smaller than what is given by the Saha-Boltzmann formula at 11,200 K. Therefore, the Doppler-broadening width dominates the lineshape of the 777 nm transition within the test time in all experiments of this study.

The spectral lineshape of absorbance α_ν for the 777 and 926 nm transitions is fitted using a Voigt function, which is the convolution of Gaussian and Lorentzian lineshapes. The MATLAB function "`lsqcurvefit`" is used to minimize the residual sum of squares of absorbance given by

$$e(\Delta\nu_d, \Delta\nu_c, A, \nu_0) = \sum_{\nu} \left(\alpha(\nu, \Delta\nu_d, \Delta\nu_c, A, \nu_0) - \alpha_m(\nu)\right)^2 \tag{6}$$

where $\alpha_m(\nu)$ is the measured absorbance for each scan, $\alpha(\nu, \Delta\nu_d, \Delta\nu_c, A, \nu_0)$ is the fitted absorbance, $\Delta\nu_d$ and $\Delta\nu_c$ are the fitted Doppler and collisional broadening, A is the fitted integrated area of absorbance, ν_0 is the fitted line-center frequency.

$$\Delta{\nu_d}^*, \Delta{\nu_c}^*, A^*, \nu_0^* = \arg \min_{\Delta\nu_d, \Delta\nu_c, A, \nu_0} e(\Delta\nu_d, \Delta\nu_c, A, \nu_0) \tag{7}$$

The Stark shift of each scan is determined by the relative line-center shift with respect to the first scan that has a reliable Voigt fit. The van der Waals broadening can be estimated from the collisional broadening of the first scan that has a reliable Voigt fit. The Stark broadening of each scan can be estimated by subtracting the van der Waals broadening from the overall collisional broadening.

C. Time-histories measurements

Number density n_4 and T_{tr} are inferred from the integrated area and Doppler broadening FWHM of the 777 nm absorbance. Number density n_6 and n_e are are inferred from the integrated area and the Stark shift of the 926 nm absorbance. Sample measurements of the raw laser intensity and absorbance at 777 and 926 nm can be found in our previous work[18]. Because of the high energy gap and the strong chemical non-equilibrium of the O(3p ^{5}P$_3$) state (relative to the ground state), the population of atomic oxygen in the O(3p ^{5}P$_3$) state is typically low (on the order of 10^{15} m^{-3}). To maintain a sufficient signal-to-noise ratio (SNR) of the 926 nm transition, the experimental temperature ($T_{5,0}$) of n_6 and n_e was limited to 10,000 K, and above.

Sample measurements of the four time-histories,n_4, n_6, n_e, and T_{tr} at $T_{5,0} = 10153$ K, $P_{5,0} = 0.5$ atm are shown in Figure 3. Errors bars in this figure represent the 95% confidence intervals of the fitted/inferred values. Also shown in Figure 3 are the simulation results of the optimized kinetic model, which are elaborated in detail in section III B.

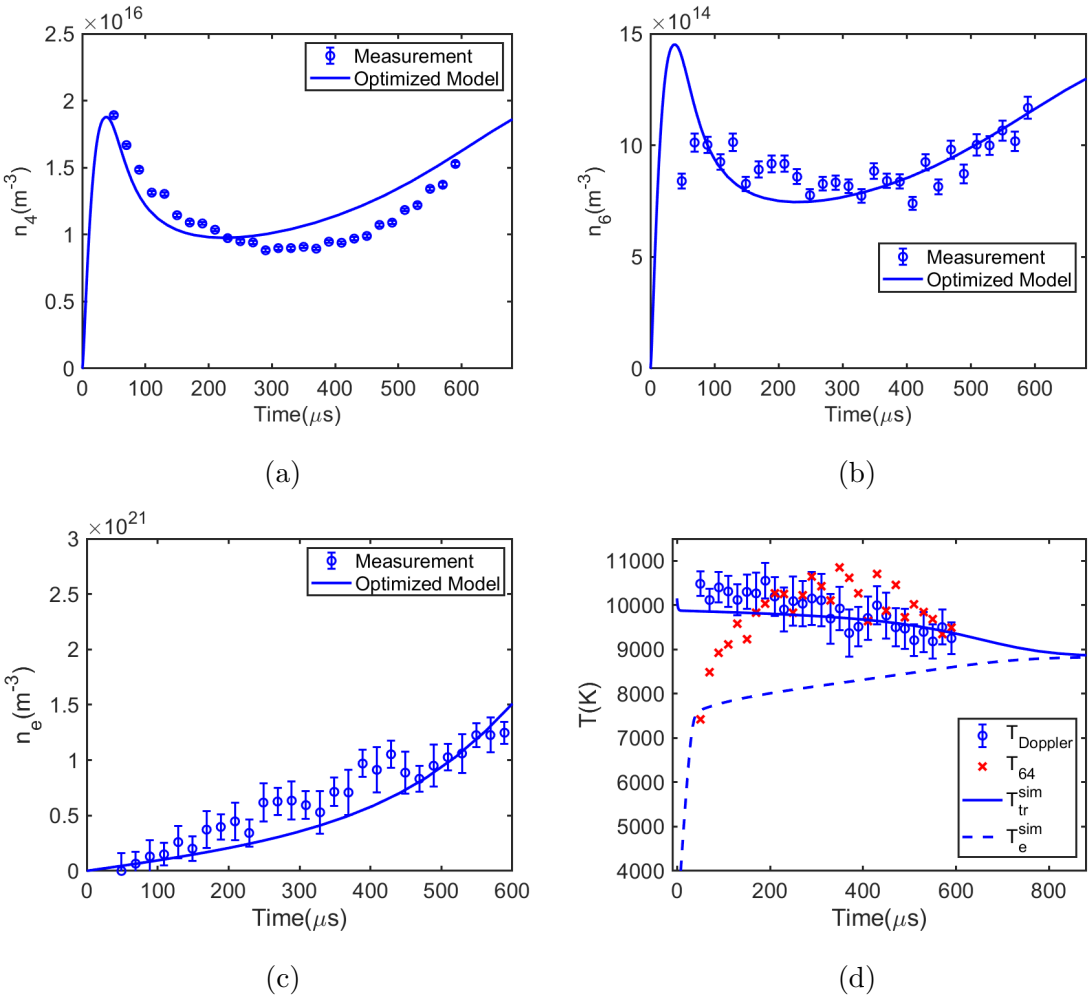

FIG. 3: Time-history measurements and model predictions of (a) population of O(3s ^{5}S^o), n_4; (b) population of O(3p ^{5}P$_3$), n_6; (c) electron number density, n_e; (d) temperature, at $T_{5,0}$ =10153 K, $P_{5,0}$ =0.49 atm. T_{Doppler} is inferred from 777 nm Doppler broadening; T_{64} is inferred from the ratio of measured populations in levels 4 and 6; $T_{\text{tr}}^{\text{sim}}, T_e^{\text{sim}}$ are model-predicted heavy-particle and electron translational temperature. Errors bars in this figure represent the 95% confidence interval of the fitted/inferred values from Voigt fits.

1. Time-history of atomic oxygen population in the O(3s $^5S^o$) and O(3p $^5P_3$) states

Figure 3a and Figure 3b show the population time-histories of atomic oxygen in the O(3s ^{5}S^o) and O(3p ^{5}P$_3$) states, obtained from the integrated area of the absorbance using Equation 1. The n_4 time-history shows three stages, dominated by the heavy-particle-impact excitation, the electron impact de-excitation and the electron impact excitation reactions, respectively, according to our model. The n_6 time-history also shows multiple stages, but not as obvious as those of n_4. The fitting error bars are larger in the n_6 measurement than the n_4 measurement because of the smaller population of atomic oxygen in the energy level 6, and therefore worse SNR for the 926 nm transition data. The measured population time-histories show that atomic oxygen in the levels 4 and 6 of are not in chemical equilibrium with atomic oxygen in the ground state, i.e. both of them deviate from the calculations from the Boltzmann distribution.

In equilibrium, the i^{th} energy level population for atomic oxygen follows a Boltzmann distribution given by

$$\frac{n_i^{\text{eq}}}{n_{\text{total}}} = \frac{g_i}{Q_O} \exp\left(-\frac{E_{i1}}{kT}\right) \tag{8}$$

where n_i^{eq} is the equilibrium population of the i^{th} energy level, g_i is the degeneracy of the i^{th} energy level, E_{i1} is the energy difference between the i^{th} energy level and the ground state atomic oxygen (hence the subscript "1"), Q_O is the partition function of atomic oxygen, T is the equilibrium temperature.

A non-equilibrium factor for the excited-state atomic oxygen is defined here to be its measured population normalized by its Boltzmann equilibrium population as calculated at the simulated translational temperature using Equation 8. For example, the non-equilibrium factor for the 4^{th} energy level is n_4/n_4^{eq}, where n_4 is the experimental measurement and n_4^{eq} is calculated using Equation 8 at the simulated translational temperature.

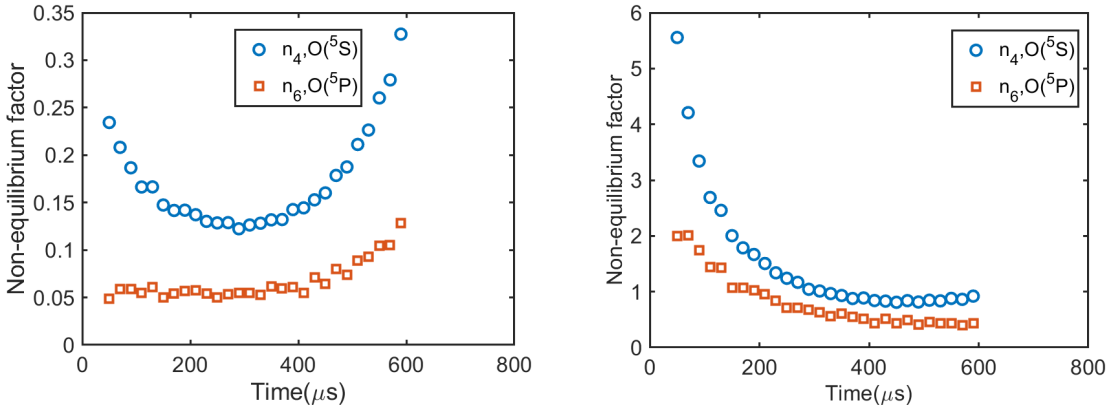

FIG. 4: Normalized population time-histories for O(3s ^{5}S^o) and O(3p ^{5}P$_3$) states at the same $T_{5,0}, P_{5,0}$ of Figure 3. (a) Normalized at the simulated heavy-particle translational temperature (b) Normalized at the simulated electron translational temperature. O* population is close to being in equilibrium with electrons at the later test time.

The non-equilibrium factors for atomic oxygen in the O(3s ^{5}S^o) and O(3p ^{5}P$_3$) states are shown in Figure 4. Figure 4a shows the population normalized by equilibrium value assuming the simulated heavy-particle translational temperature, T_{tr}, in Equation 8. The O* population time histories are smaller than the equilibrium values assuming T_{tr}. The population of atomic oxygen in the O(3p ^{5}P$_3$) state deviates more from its equilibrium value than the O(3s ^{5}S^o) state, presumably due to its larger energy gap and lower excitation rates. After around 400 μs, the population of atomic oxygen in both states rise towards equilibrium (equivalently, non-equilibrium factors increase towards 1) because of the increase in electron translational temperature and electron number density. Figure 4b shows the population normalized by equilibrium value assuming the simulated electron translational temperature, T_{e}, in Equation 8. The O* states are close to being in equilibrium with electrons at later test time and

their non-equilibrium factors are close to 1. This is because at later test time there are sufficient electrons and T_e is large enough. The electrons dominate the collisional excitation of O*. The initial non-equilibrium factor is larger than 1 in Figure 4b because of the low initial electron temperature (300K) in the model.

2. Electron number density time-history

Electron number density, n_e, is one of the most important quantities in the kinetic model because electrons are much more efficient in exciting the atomic species compared with heavy particles. By utilizing the laser diagnostic technique recently developed in our group[18], electron number density is inferred from the 926 nm absorbance Stark shift; the corresponding n_e time-history for $T_{tr,0} = 10,153$K in [18] is reproduced in Figure 3c.

The direct measurement of n_e time-history in the current study verifies that electrons are produced at a rate much faster than the prediction considering only Ar ionization. This will be further elaborated in section III B.

3. Temperature time-history

Figure 3d shows the Doppler temperature, T_{Doppler}, inferred from 777 nm Doppler broadening FWHM using Equation 3; the population temperature, T_{64}, calculated from the population ratio of levels 4 and 6 using Equation 8; and the model-predicted (see section III B) heavy particle translational temperature, $T_{\text{tr}}^{\text{sim}}$ and the electron translational temperature, T_e^{sim}.

The measured Doppler temperature generally agrees with the simulated translational temperature within the $\pm 5\%$ fitting error bar. The simulated translational temperature first drops $\sim$300K from the initial $T_{5,0}$ of 10153 K due to the endothermic O_2 dissociation, then further drops $\sim$800K due to the endothermic Ar ionization

within the test time. At the same time, the electron temperature increases continuously within the test time until reaching thermal equilibrium with the heavy particle translational temperature at ∼8900 K beyond our test time.

The population temperature T_{64} is calculated from the population n_4, n_6 using

$$\frac{n_6}{n_4} = \frac{g_6}{g_4} \exp\left(-\frac{E_{64}}{kT_{64}}\right) \tag{9}$$

where g_4, g_6 are the degeneracy of atomic oxygen in the energy levels 4 and 6, and n_4, n_6 are the measured population of atomic oxygen in the energy levels 4 and 6.

The population temperature T_{64} is lower than the translational temperature in the first 100 μs because population of atomic oxygen in the level 4 increases faster than that at level 6 due to heavy-particle excitation rate constant k_{14} is larger than k_{16}. From around 100 μs to the end of the test time, T_{64} is approximately in agreement with the heavy particle translational temperature ($T_{\mathrm{tr}}^{\mathrm{sim}}$ in Figure 3d). This indicates that the relative populations of atomic oxygen in the energy levels 4 and 6 are close to those calculated from the Boltzmann distribution at the corresponding translational temperature, although Figure 4 shows that they are not individually in chemical equilibrium with the ground state. These results suggest that reaction X in Table II, the heavy-particle-impact collisional excitation/de-excitation, is very fast and in partial equilibrium, although the whole system is not in chemical equilibrium. These observations provide insight regarding tuning of the rate constant k_{46} in the kinetic model in section III B.

D. Uncertainty analysis

The shock velocity error for the current study is 0.5%, which corresponds to a temperature uncertainty of about 1%. The pressure rise within the test time is mitigated by using a driver insert [24] to be below 5% within the test time for most cases. The rise time of the Kistler pressure transducer is less than 5 μs. Uncertainty

of time zero for the experiment is less than 5μs.

The uncertainty analysis of the electron number density is discussed in reference [18]. Line-center shift uncertainties from the Voigt-fit and the systematic experimental effects are on the order of 15%. The uncertainty in the Stark shift formula is hard to quantify without a detailed quantum mechanical calculation and other n_e diagnostics to validate. A discrepancy of 50% was reported previously between the measured and the predicted Stark shift for some atomic oxygen transitions[25].

The fitting uncertainties for n_4, n_6 and $T_{\rm tr}$ are on the order of 1%, 5%, 5%, respectively. Considering other systematic experimental effects, the uncertainties for these quantities are estimated to be on the order of 5%-10%.

III. MODELING RESULTS

A. The two-temperature collisional-radiative (CR) model

1. Collisional and radiative processes

The current study extends a previous collisional-radiative model[17] to include atomic oxygen in the O(3p ^{5}P$_3$) state and seven more reactions involving atomic oxygen in this state. As shown in Table II, fifteen collisional and radiative processes are included in the current model: O_2 dissociation, electron/heavy-particle impact excitation of atomic oxygen to O(3s ^{5}S^o) and O(3p ^{5}P$_3$) states, electron/heavy-particle collisions between atomic oxygen in the O(3s ^{5}S^o) and O(3p ^{5}P$_3$) states, electron/heavy-particle impact ionization of atomic oxygen in the O(3s ^{5}S^o) and O(3p ^{5}P$_3$) states, electron/heavy-particle impact ionization of Ar, spontaneous emission of atomic oxygen in the O(3s ^{5}S^o) and O(3p ^{5}P$_3$) states. The formulas for reaction rate constants are adapted from the literature and presented in Table II, and the calculated rate constants from the literature are referred to as the "nominal values" and used as the initial

TABLE II: Collisional and radiative processes included in the current model. The pre-factors of the twelve atomic collisional excitation rate constants, $\exp(F_i), i = 1, \ldots, 12$, are optimized to match the measured time-histories of $n_4, n_6, n_e, T_{\rm tr}$ using the stochastic gradient descent algorithm and reported in Table III.

Label	Reaction	Forward Rate constant Formula	Reference
I	$Ar + O_2 = Ar + 2O(g)$	$k_{dis} = 3.9 \times 10^{12} (T_{\rm tr})^{-1} \exp(-59380K/T_{\rm tr}) \mathrm{m}^3/\mathrm{mol/s}$	[26]
II	$Ar + O(g) = Ar + O(^5S^0)$	$k_{14} = \exp(F_1) \times 2\sqrt{\frac{2}{\pi m_{Ar,O}}} \beta_{14} (kT_{\rm tr})^{1/2} (E_{41} + 2kT_{\rm tr}) \exp(-\frac{E_{41}}{kT_{\rm tr}}) \mathrm{m}^3/\mathrm{s}$	[17]
III	$e^- + O(g) = e^- + O(^5S^0)$	$k^e_{14} = \exp(F_2) \times 8.629 \times 10^{-6} / g_1 / T_e^{1/2} \gamma_{14} \exp(-\frac{E_{41}}{kT_e}) \mathrm{m}^3/\mathrm{s}$	[27]
IV	$Ar + Ar = Ar + Ar^+ + e^-$	$k^M_{Ar,c} = \exp(F_3) \times 1.68 \times 10^{-26} T_{\rm tr}^{1.5} (\frac{\theta_{A^*,1}}{T_{\rm tr}} + 2) \exp(-\frac{\theta_{A^*,1}}{T_{\rm tr}}) \mathrm{m}^3/\mathrm{s}$	[28, 29]
V	$e^- + Ar = e^- + Ar^+ + e^-$	$k^e_{Ar,c} = \exp(F_4) \times 3.75 \times 10^{-22} T_e^{1.5} (\frac{\theta_{A^*,1}}{T_e} + 2) \exp(-\frac{\theta_{A^*,1}}{T_e}) \mathrm{m}^3/\mathrm{s}$	[28, 29]
VI	$Ar + O(^5S^0) = Ar + e^- + O^+$	$k^M_{4c} = \exp(F_5) \times 64\pi a_0^2 (\frac{E^H}{E_{4c}})^2 (\frac{kT_{\rm tr}}{\pi m_{Ar}})^{\frac{1}{2}} \zeta^2 \frac{m_e m_{Ar}}{m_H (m_e + m_{Ar})} \psi(w_{4c})\ \mathrm{m}^3/\mathrm{s}$	[30]
VII	$e^- + O(^5S^0) = e^- + e^- + O^+$	$k^e_{4c} = \exp(F_6) \times 4\pi a_0^2 (\frac{8kT_e}{\pi m_e})^{\frac{1}{2}} \alpha (\frac{E_{4c}}{kT_e})^2 I_2(a_{4c})\ \mathrm{m}^3/\mathrm{s}$	[1]
VIII	$Ar + O(g) = Ar + O(3p^5P_3)$	$k_{16} = \exp(F_7) \times 2\sqrt{\frac{2}{\pi m_{Ar,O}}} \beta_{16} (kT_{\rm tr})^{1/2} (E_{61} + 2kT_{\rm tr}) \exp(-\frac{E_{61}}{kT_{\rm tr}}) \mathrm{m}^3/\mathrm{s}$	[17]
IX	$e^- + O(g) = e^- + O(3p^5P_3)$	$k^e_{16} = \exp(F_8) \times 8.629 \times 10^{-6} / g_1 / T_e^{1/2} \gamma_{16} \exp(-\frac{E_{61}}{kT_e}) \mathrm{m}^3/\mathrm{s}$	[27]
X	$Ar + O(3p^5P_3) = Ar + e^- + O^+$	$k^M_{6c} = \exp(F_9) \times 64\pi a_0^2 (\frac{E^H}{E_{6c}})^2 (\frac{kT_{\rm tr}}{\pi m_{Ar}})^{\frac{1}{2}} \zeta^2 \frac{m_e m_{Ar}}{m_H (m_e + m_{Ar})} \psi(w_{6c})\ \mathrm{m}^3/\mathrm{s}$	[30]
XI	$e^- + O(3p^5P_3) = e^- + e^- + O^+$	$k^e_{6c} = \exp(F_{10}) \times 4\pi a_0^2 (\frac{8kT_e}{\pi m_e})^{\frac{1}{2}} \alpha (\frac{E_{6c}}{kT_e})^2 I_2(a_{6c})\ \mathrm{m}^3/\mathrm{s}$	[1]
XII	$Ar + O(^5S^0) = Ar + O(3p^5P_3)$	$k_{46} = \exp(F_{11}) \times 2\sqrt{\frac{2}{\pi m_{Ar,O}}} \beta_{46} (kT_{\rm tr})^{1/2} (E_{64} + 2kT_{\rm tr}) \exp(-\frac{E_{64}}{kT_{\rm tr}}) \mathrm{m}^3/\mathrm{s}$	[17]
XIII	$e^- + O(^5S^0) = e^- + O(3p^5P_3)$	$k^e_{46} = \exp(F_{12}) \times 8.629 \times 10^{-6} / g_4 / T_e^{1/2} \gamma_{46} \exp(-\frac{E_{64}}{kT_e}) \mathrm{m}^3/\mathrm{s}$	[27]
XIV	$O(^5S^0) \rightarrow O(g) + \mathrm{h}\nu$	$A_{41} = 5.56 \times 10^3 \mathrm{s}^{-1}$	[31]
XV	$O(3p^5P_3) \rightarrow O(^5S^0) + \mathrm{h}\nu$	$A_{64} = 3.69 \times 10^7 \mathrm{s}^{-1}$	[1, 31]

guesses for the optimization procedure described in algorithm 1. Each nominal rate

constant for the atomic collision is multiplied by a pre-factor $\exp(F_i), i = 1, \ldots, 12$ in Table II to match the measured time histories. In section III B, algorithm 1 is used to optimize the logarithm of these pre-factors, i. e., F_i.

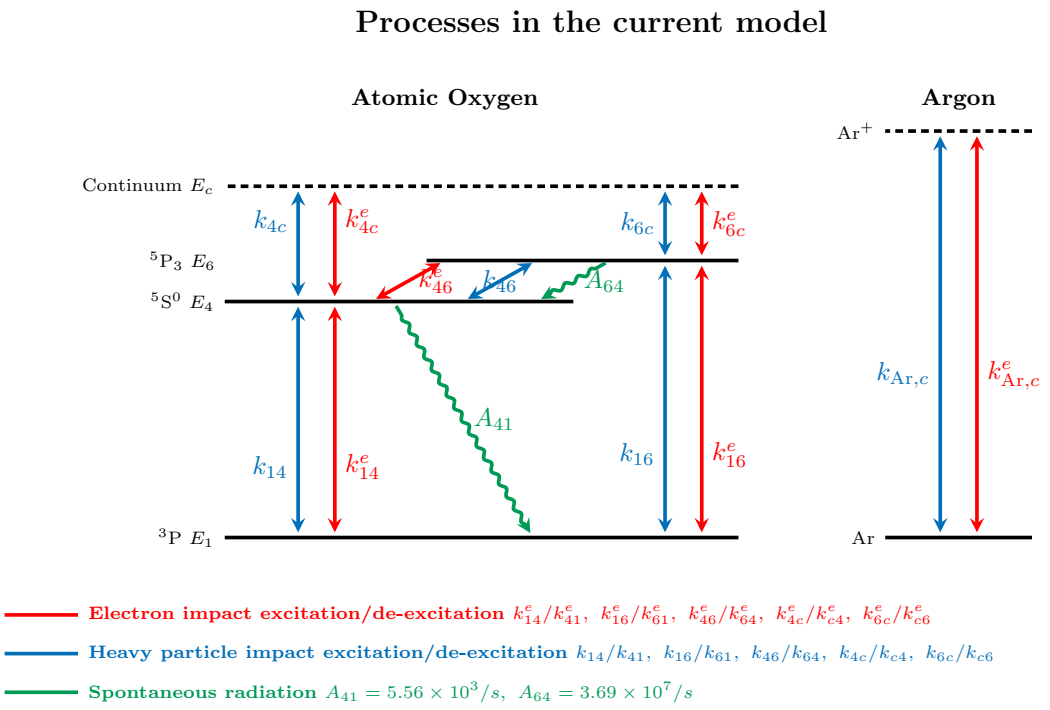

FIG. 5: Twelve collisional rate constants and two spontaneous emission rates in the current model. Two-way arrows indicate the collisional excitation and de-excitation reactions. One-way arrows indicate spontaneous emission. Blue/red/green lines represent heavy particle impact/electron impact collisions and spontaneous emission.

Figure 5 shows the energy diagram and 14 collisional and radiative processes of atomic oxygen. We follow the same notation as in [17] and use subscript "1,4,6" in the formulas for reaction rate constants to denote the ground state, O(g), the excited O(3s ^{5}S^o) and O(3p ^{5}P$_3$) states of atomic oxygen, respectively. The superscript "e" denotes the reaction rate constants for electron impact reactions. Detailed discussions for most of the rate formulas can be found in a previous work[17]. The additional

reaction rate constants involving atomic oxygen level 6 are discussed below.

The rate constant of heavy-particle excitation of atomic oxygen to the O(3p $^5P_3$) state, i.e. k_{16}, is assumed to have the same form as k_{14} (the excitation reaction rate constant to O(3s $^5S^o$) state)[17, 32], with the exception that the activation energy is the energy gap between the O(3p $^5P_3$) state and the ground state. Similarly, the cross coupling rate between levels 4 and 6, k_{46}, is assumed to have the same form with k_{14} with the exception of using the energy gap between energy levels 4 and 6 as the activation energy. The cross-sectional slope constant, β_{46}, β_{16} are set to be equal to β_{14} in the nominal values in Table II. It is of note that the cross-sectional slope constant is likely to be negatively correlated to the energy gap[33] and some of the nominal values in Table II adapted from the empirical rate constant formulas, which are also used as initial guesses in the optimization procedure (algorithm 1), may be far away from the optimized value as suggested by the large values of some optimized pre-factors shown in Table III. For instance, the cross-sectional slope constant, β_{46}, is likely to be larger than the cross-sectional slope constant of β_{14} because the energy gap between levels 4 and 6 is smaller and the transition from level 4 to 6 is spin-allowed while that from level 1 to 4 is spin-forbidden. Correspondingly, the pre-factor of k_{46} is optimized to be 6200 as shown in Table III, indicating the initial guess of k_{46} is under-estimated, probably due to $\beta_{46}/\beta_{14} \gg 1$. It will be further elaborated in section III B 1.

The rate constant of electron impact excitation from ground state to O(3p $^5P_3$) state, k_{16}^e, is assumed to take the same form as that of the electron impact excitation reaction from ground state to O(3s $^5S^o$)[17, 32], with the effective collision strength $\gamma_{16} = 1.76 \times 10^{-1}$[27]. γ_{46} is set to be equal to the nominal values of γ_{14} as shown in Table II.

2. Species and energy conservation equations

The temporal variation in species number density is governed by a set of ordinary differential equations (ODE) similar to that in [17]. The reaction rate constants involving atomic oxygen in the O(3p ^{5}P$_3$) state are included in the ODE. For example, the species conservation equation for atomic oxygen in the O(3p ^{5}P$_3$) state is given by

$$\begin{aligned}\frac{\partial n_6}{\partial t} &= \dot{n}_6 \\ &= \left(k_{16} n_{O(g)} n_{Ar} + k_{16}^e n_e n_{O(g)} + k_{46} n_{O(^5S^0)} n_{Ar} + k_{46}^e n_e n_{O(^5S^0)} + k_{c6}^e n_{O^+} n_e^2 + k_{c6}^M n_{O^+} n_e n_{Ar}\right) \\ &- \left(k_{61} n_6 n_{Ar} + k_{61}^e n_6 n_e + k_{64} n_6 n_{Ar} + k_{64}^e n_6 n_e + k_{6c}^e n_e n_6 + k_{6c}^M n_6 n_{Ar}\right) \\ &- \Lambda_{64} A_{64} n_6\end{aligned} \tag{10}$$

where the source term $\dot{n}_6$ is the volumetric production rate of atomic oxygen in the energy level 6. All the rate constants are listed in Table II. The escape factor[34], Λ_{64}, is negatively correlated to the absorption coefficient of the transition from energy level 4 to 6. In general, $\Lambda_{64} \approx 1$ for a small absorption coefficient and $\Lambda_{64} \approx 0$ for large absorption coefficient ($k \gg 1$). We assess the transition from energy level 6 to 4 to be optically thin, i.e. with small absorption coefficient, because the mole fraction of atomic oxygen in the energy level 4 is generally below 1 ppm in the current study. Therefore, the escape factor Λ_{64} is set to be 1. One might expect a stronger depletion of atomic oxygen in the energy level 6 than that at level 4 due to the four-orders-of-magnitude larger spontaneous emission rate of A_{64} compared with A_{41} as shown in Table II. However, the current measurement results in section II C 1 and section II C 3 show that atomic oxygen in the levels 4 and 6 approximately follow the Boltzmann distribution at the translational temperature, indicating a large heavy-particle-impact cross-coupling rate between levels 4 and 6.

The electron and heavy-particle translational temperatures are used in the rate constant formulas that involve electrons and only heavy particles, respectively. The two temperatures are solved from the energy conservation equations similar to those in [17], but including the energy source terms due to reactions involving atomic oxygen of the O(3p $^5P_3$) state.

The energy conservation equation for electron is given by Panesi[1], Hoffert[28] and Kapper[35]:

$$\begin{aligned} n_e \frac{3}{2} k \frac{\partial T_e}{\partial t} &= \left[\frac{\partial E_e}{\partial t}\right]_{\text{Ion}} + \left[\frac{\partial E_e}{\partial t}\right]_{\text{Exc}} + \left[\frac{\partial E_e}{\partial t}\right]_{\text{Coll}} + \left[\frac{\partial E_e}{\partial t}\right]_{\text{Brem}} \\ &= -\dot{n}^e_{Ar,c} E_{Ar,c} - \dot{n}^e_{4c}(E_{O,c} - E_{41}) - \dot{n}^e_{6c}(E_{O,c} - E_{61}) - \dot{n}^e_{14} E_{41} - \dot{n}^e_{16} E_{61} \\ &- \frac{2m_{Ae}}{m_e + m_A} \frac{3}{2} (\nu_{Ae} + \nu_{A^+e}) n_e k (T_e - T_{\text{tr}}) - 1.42 \times 10^{-40} Z^2_{eff} T_e^{1/2} n_+ n_e \end{aligned} \tag{11}$$

The five terms in the first line of Equation 11 represent the loss of electron sensible energy due to electron impact Ar and O ionization, electron impact excitation of O atoms, Ar-electron and Ar^+-electron collisions and Bremsstrahlung emission; $\dot{n}^e_{Ar,c}, \dot{n}^e_{4c}, \dot{n}^e_{6c}$ are the electron impact ionization rates of Ar, atomic oxygen in the O(3s $^5S^o$) and O(3p $^5P_3$) states; $E_{Ar,c}$ and $E_{O,c}$ are the ionization energy of Ar and O atom; $\dot{n}_i$ is the volumetric reaction rate for producing species i[17]. The collision frequencies of Ar-electron and Ar^+-electron, i.e. ν_{Ae} and ν_{A^+e}, are given in reference [17]; $Z_{eff} = 1.67$[35].

The heavy particle energy conservation equation is given by [17]

$$
\begin{aligned}
&\left(\sum_{i\in\Pi} n_i \frac{3}{2}k + n_{O_2} c_{v,O_2}\right)\frac{\partial T_{\rm tr}}{\partial t} \\
&= -\sum_{i\in\Pi}\dot{n}_i\left(\frac{3}{2}kT_{\rm tr} + E_{{\rm chem},i}\right) - \dot{n}_{O_2}(E_{sens,O_2} + E_{{\rm chem},O_2}) - \dot{n}_e\left(\frac{3}{2}kT_e + E_{{\rm chem},e}\right) \\
&+ \dot{n}^e_{Ar^+}E_{Ar,c} + \dot{n}^e_{4c}(E_{O,c} + E_{41}) + \dot{n}^e_{6c}(E_{O,c} - E_{41}) + \dot{n}^e_{14}E_{41} + \dot{n}^e_{16}E_{61} \\
&+ \frac{2m_{Ae}}{m_e + m_A}\frac{3}{2}(\nu_{Ae} + \nu_{A^+e})n_e k(T_e - T_{\rm tr}) - A_{41}E_{41}n_{O(^5S^0)} - A_{64}E_{64}n_{O(^5P_3)}
\end{aligned}
\tag{12}
$$

where Π includes atomic oxygen in the O(g), O($^5S^0$), O($^5P_3$) states, Ar, Ar^+, O^+. $\dot{n}_i$ is the volumetric reaction rate for producing species i[17]. The chemical energy for the atomic species i, $E_{{\rm chem},i}$, and for molecular oxygen, $E_{{\rm chem},O_2}$, are taken from reference [36]. The sensible energy for O_2, $E_{{\rm sens},O_2} = n_{O_2}(H_{{\rm sens},O_2} - kT_{\rm tr})$, where $H_{{\rm sens},O_2}$ is the enthalpy per molecule calculated using the NASA Glenn coefficients [36].

B. Optimization of the CR model

1. *Optimization procedure using SGD algorithm of the twelve rate constant pre-factors*

Twelve logrithmic pre-factors of the collisional reaction rate constants in Table II, i.e., $F_i, i = 1, \ldots, 12$, are optimized by minimizing the cost function defined by Equation 13 using the stochastic gradient descent (SGD), as described in algorithm 1.

$$
\begin{aligned}
{\rm Cost}(F_1, \ldots, F_{12}) = &\left(\frac{n_4^{meas} - n_4^{sim}}{||n_4^{meas}||_2}\right)^2 + \left(\frac{n_6^{meas} - n_6^{sim}}{||n_6^{meas}||_2}\right)^2 \\
&+ \left(\frac{n_e^{meas} - n_e^{sim}}{||n_e^{meas}||_2}\right)^2 + \left(\frac{T_{tr}^{meas} - T_{tr}^{sim}}{||T_{tr}^{meas}||_2}\right)^2
\end{aligned}
\tag{13}
$$

where $F_1, \ldots, F_{12}$ are the logarithm of the rate-constant pre-factors in Table II; $n_4^{meas}, n_6^{meas}, n_e^{meas}, T_{tr}^{meas}$ are the measured time-histories for the population of the atomic oxygen in the O(3s ^{5}S^o), O(3p ^{5}P$_3$) states, the electron number density and

the translational temperature; the superscript "sim" denotes the simulation results from the model. Normalization by the 2-norm of the measured time-history vectors accounts for the difference in magnitude of the residuals from the four different quantities.

Result: Optimized F^* for the logarithm of the pre-factor for the twelve reaction rate constants in Table II and Table III

for *each run of stochastic gradient descent* **do**

Initialization: random initialize the twelve pre-factors using the initial guess given in Table III;

for *epoch = 1 : epoch*$_{max}$ **do**

for *each experiment* **do**

1. calculate reaction rate constants from current pre-factors
2. evaluate cost for the current model using Equation 13
3. evaluate gradient numerically $g' = \nabla_F \text{Cost}$
4. update F by $F = F - \frac{\alpha}{N_t} g'$, where α is the learning rate and N_t is the number of data points for one measured time-history.

end

end

end

pick the best set of optimized parameters corresponding to the smallest cost and set F^* correspondingly.

Algorithm 1: Optimization procedure for the logarithm of pre-factors in Table II and Table III, F^*, using stochastic gradient descent algorithm.

For each shock in each epoch of the SGD procedure algorithm 1, the logarithm of pre-factors, i.e. $F_i (i = 1, \ldots, 12)$ are updated one time using the gradient of the

cost function. The benefits of optimizing the logarithm of pre-factors are twofold. Firstly, since the reaction rate constants span multiple orders of magnitude, taking logarithms improves numerical stability. Secondly, by updating the pre-factors on log-scale, i.e. updating F_i, we avoid dealing with the constraints that all reaction rate constants must be positive as $\exp(F_i)$ is always positive. The gradient of the cost function with respect to each logarithmic pre-factor F_i is numerically evaluated using Equation 13 by perturbing F_i by a small fraction (e.g. $\delta = 1\%$), i.e. gradient

$$g_i' = \frac{\text{Cost}(F_i + \delta F_i; F_j, \forall j \neq i) - \text{Cost}(F_i - \delta F_i; F_j, \forall j \neq i)}{2\delta F_i} \tag{14}$$

The algorithm generally converges to a local optimum after 50 epochs.

The SGD algorithm is run multiple times (e.g. five times in the current work) as described in algorithm 1, each time with a set of random initialization of rate-constant pre-factors given by Table III. The random initialization for most F_i are uniformly distributed within [-1,1], therefore the initial guesses for pre-factors are $\sim \exp(U(-1,1))$ where $U(-1,1)$ is the uniform distribution between -1 to 1. The optimized pre-factor values for these rate constants are generally on the order of 1 as shown in Table III. The set of rate-constant pre-factors corresponding to the minimum cost among the five runs are reported as the "optimized pre-factors" in Table III.

Three pre-factors in Table III are initialized with $\sim \exp(U(2.5,4.5))$, namely, the rate constants $k_{Ar,c}, k^e_{Ar,c}$ and k_{46}. The large initial guesses for the pre-factors of the two Ar ionization rate constants are chosen to improve the speed of converge. The faster electron number density production rate in the measurement yields pre-factors for $k_{Ar,c}, k^e_{Ar,c}$ on the order of 24 and 25, i.e., 24 and 25 times larger than the nominal values reported by Kelly's measurements[29]. The large discrepancy between the current inferred rates and the well-established rate constants is likely due to the simplifications in the model to neglect critical oxygen ionization processes, and/or ionization of impurities in the shock tube.

TABLE III: Random initialization and optimized values of rate constant pre-factors. Optimized pre-factors are chosen with the minimal cost in multiple runs of SGD algorithm as described in algorithm 1.

Rate Constant	Reaction	Range of Pre-factors Initial Guess	Optimized Pre-factors
k_{14}	$Ar + O(g) = Ar + O(^5S^0)$	[exp(-1),exp(1)]	0.5
k^e_{14}	$e^- + O(g) = e^- + O(^5S^0)$	[exp(-1),exp(1)]	0.3
$k^M_{Ar,c}$	$Ar + Ar = Ar + Ar^+ + e^-$	[exp(2.5),exp(4.5)]	24
$k^e_{Ar,c}$	$e^- + Ar = e^- + Ar^+ + e^-$	[exp(2.5),exp(4.5)]	25
k^M_{4c}	$Ar + O(^5S^0) = Ar + e^- + O^+$	[exp(-1),exp(1)]	0.6
k^e_{4c}	$e^- + O(^5S^0) = e^- + e^- + O^+$	[exp(-1),exp(1)]	2.5
k_{16}	$Ar + O(g) = Ar + O(3p^5P_3)$	[exp(-1),exp(1)]	0.4
k^e_{16}	$e^- + O(g) = e^- + O(3p^5P_3)$	[exp(-1),exp(1)]	0.4
k^M_{6c}	$Ar + O(3p^5P_3) = Ar + e^- + O^+$	[exp(-1),exp(1)]	0.3
k^e_{6c}	$e^- + O(3p^5P_3) = e^- + e^- + O^+$	[exp(-1),exp(1)]	3.7
k_{46}	$Ar + O(^5S^0) = Ar + O(3p^5P_3)$	[exp(2.5),exp(4.5)]	6200
k^e_{46}	$e^- + O(^5S^0) = e^- + O(3p^5P_3)$	[exp(-1),exp(1)]	0.4

Besides the two Ar ionization rates, the pre-factor of the cross coupling rate constant between levels 4 and 6, k_{46}, is also uniformly randomly initialized to be within $\exp(U(2.5, 4))$ as shown in Table III. A large pre-factor of k_{46} is expected for the following three reasons. Firstly, large collisional excitation rate constants are needed to compensate the large spontaneous emission rate A_{64}. Figure 6 illustrates this effect.

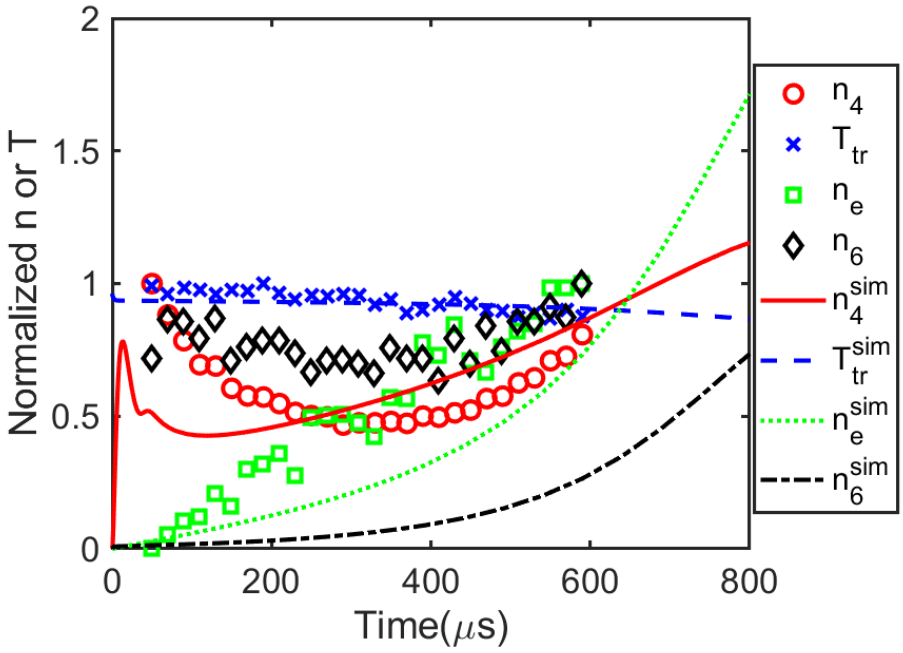

FIG. 6: Normalized time-histories at the same $T_{5,0}, P_{5,0}$ of Figure 3. Circles: time-history measurements normalized by their maximum. Lines: normalized model predictions using nominal rate constants in Table II, i.e., pre-factors of $\exp(F_i)$ are set to $1(F_i{=}0)$.

It shows the time-history measurements normalized by the maximum measurement values, as well as the normalized model-predicted time-histories using the nominal rate constant values in Table II, i.e. pre-factors F_is are set to be 1. It is of note that the nominal rate constants adapted from the previous model were developed by matching only the time-history measurements of atomic oxygen in the O(3s ^{5}S^o) state and applicable over 8,000 - 10,000 K [17]. Small discrepancies between the current measurement of n_4 and the simulation with the nominal rate constants could be due to the extension of the temperature range. The large discrepancy between the simulated and the measured n_6 within the test time is caused by the large spontaneous emission rate (i.e. large A_{64} in Table II), which dominates the n_6 time-history over the

other collisional excitation reactions (correspondingly, $k_{16}, k_{16}^e, k_{46}, k_{46}^e$) in the model. This discrepancy indicates that the collisional excitation rate constants are larger than their nominal values. The population temperature T_{64} in Figure 3d is close to the heavy-particle translational temperature instead of the electron temperature, indicating the heavy-particle cross coupling reactions between atomic oxygen levels 4 and 6 are in partial equilibrium, i.e., large k_{46}. Secondly, the theoretical prediction of k_{46} is not as well-established as other rate constants involving ground-state atomic oxygen and electrons and likely to be under-estimated as explained in section III A 1. Thirdly, atomic oxygen in the other excited states besides level 1, 4, 6 (such as level 5, 3, 2, and other states not included in the current kinetic model) could also contribute to the collisional excitation of atomic oxygen in the level 6. Such effects are also incorporated into the pre-factor of k_{46} in the current study.

2. Optimization results of twelve rate constant pre-factors

Figure 7 shows the cost vs the epoch number of the SGD algorithm for five different initializations of the rate constant pre-factors. An epoch is defined as one training pass through all experimental data. The algorithm generally converges after 10 epochs and costs from all five runs are close after 50 epochs of training.

Table III shows the "optimized" rate constants pre-factors, which gives the minimum cost at the last epoch among the five runs. The majority of these rate-constant pre-factors are on the order of 1. The heavy-particle and electron impact Ar ionization rate constants are optimized to be 24 and 25 times larger than their nominal values measured by Kelly, et al.[29], which presumably caused by the model simplification of neglecting critical oxygen ionization and systematic experimental effects such as ionization from impurities as explained before.

The current optimized value of heavy-particle collisional transfer rate constant k_{46}, although multiplied by a seemingly large pre-factor of 6200, is consistent with

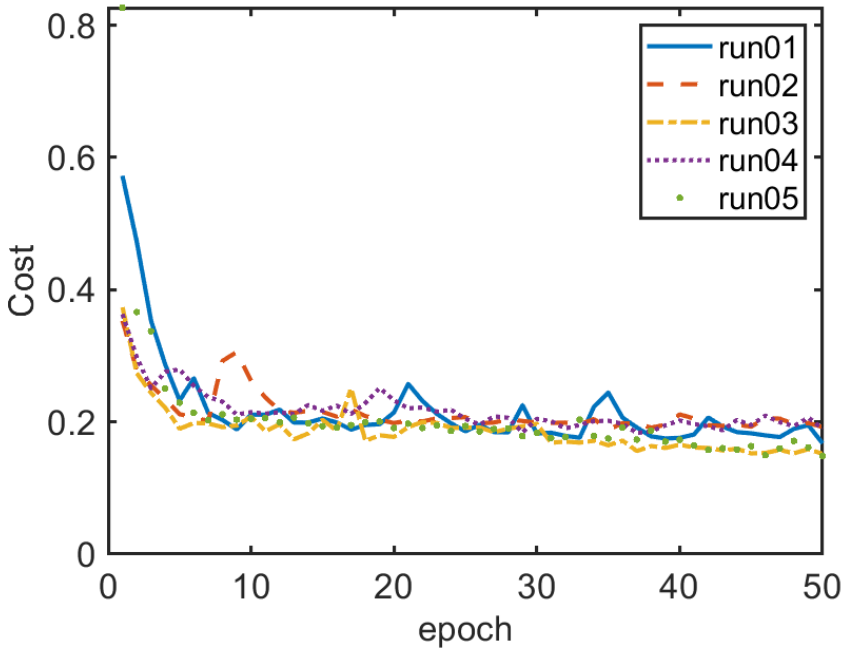

FIG. 7: Trajectory of the cost function against epoch number (one epoch is one pass through all experimental data) using SGD algorithm. The set of rates with the minimum cost are reported in Table III. Each run has a different set of random initialization as described in Table III.

Dagdigian's previous measurements[37] of the collisional transfer rate from atomic oxygen in the level 7 (O(3p ^{3}P)) to level 6 (O(3p ^{5}P)). Dagdigian et al.[37] measured this rate constant by collisions with O_2, N_2 to be $k_{76}(O_2) = 6 \times 10^{-17}, k_{76}(N_2) = 2 \times 10^{-17}$ m^3/s at room temperature. Considering that the Ar-O collisional excitation is likely to be less efficient compared with O_2-O collisional excitation, but the current temperatures are approximately 37 times higher than room temperature, the current optimized value of heavy-particle cross-coupling rate constant of $k_{64}(\mathrm{Ar}) = 6.7 \times 10^{-17}$ m^3/s at 11209 K seems consistent with Dagdigian's measurements. It is of note that the hard-sphere collisional rate constant is 1.3×10^{-15} m^3/s at 11209K for Ar-O collisions.

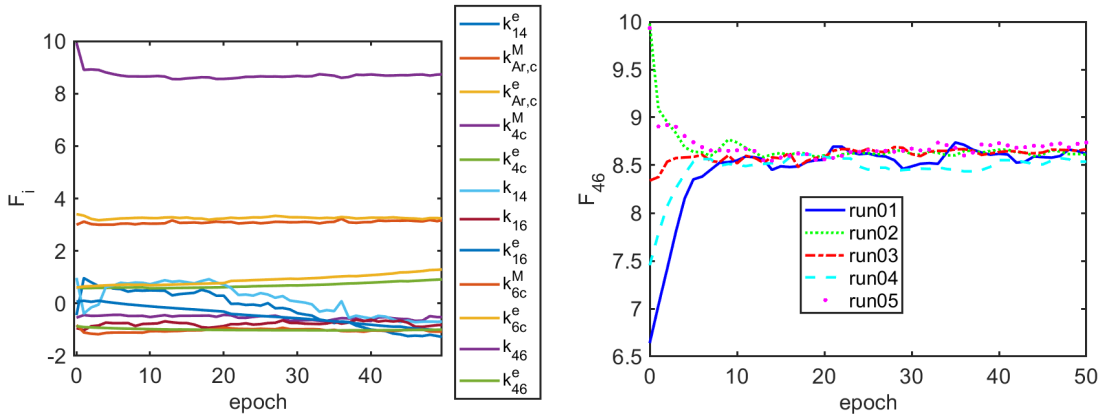

(a) (b)

FIG. 8: (a) Updates of the twelve rate-constant logarithmic pre-factors against epoch number for the run of SGD with the minimum cost. The top three lines show pre-factors for rate constants $k_{46}, k^e_{Ar,c}, k^M_{Ar,c}$ are much larger than 1. Other pre-factors are on the order of 1. (b) Updates of k_{46} logarithmic pre-factor for five different SGD runs.

Figure 8 shows the updates to individual rate constant logarithmic pre-factors by the SGD algorithm. Figure 8a shows the trajectory of twelve logarithmic pre-factors vs epoch number. The largest three rate-constant logarithmic pre-factors, i.e. $k_{46}, k_{Ar,c}, k^e_{Ar,c}$, converge within 10 epochs. Figure 8b shows the updates to the logarithmic pre-factor of k_{46} against epoch number for five SGD runs with different random initialization. In all five runs, the logarithmic pre-factor of k_{46} converges to approximately the same value after 10 epochs. It is of note that not all logarithmic pre-factors converge to the same values for different initialization, especially for those with very small sensitivity coefficients as defined in the next section. The current algorithm provides a method to determine a set of rate constants that can be used to model atomic oxygen collisional-excitation kinetics given the measured time histories.

Figure 9 shows the comparison between the measurements and the simulations

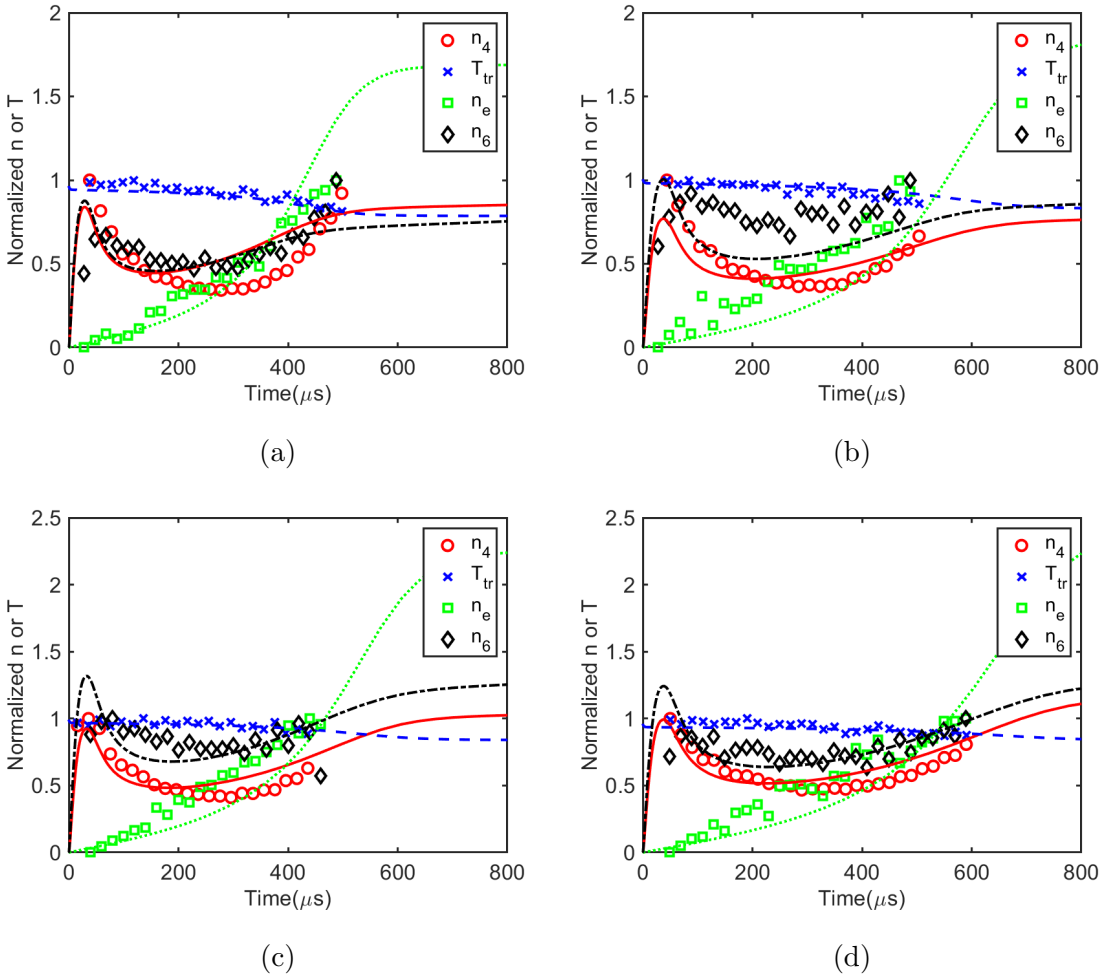

FIG. 9: Time-history measurements (symbols) and simulations (lines) with the optimized rate constants in Table III for $n_4, n_6, n_e, T_{\rm tr}$ normalized by their maximum measured values. (a) $T_{5,0} = 11209$ K, $P_{5,0} = 0.37$ atm, (b) $T_{5,0} = 10923$ K, $P_{5,0} = 0.33$ atm, (c) $T_{5,0} = 10623$ K, $P_{5,0} = 0.44$ atm, (d) $T_{5,0} = 10153$ K, $P_{5,0} = 0.49$ atm. The line style has the same meaning with Figure 6.

(using optimized rate constants) for the time-histories of $n_4, n_6, n_e, T_{\rm tr}$ normalized by their maximum measured values over $T_{5,0}$ from 10,100 to 11,200 K. The model predictions show reasonably good agreement with the data in most cases. The absolute

values of the time-histories are reported in section A for use by others seeking to model our data. The model predictions of n_4 after 200 μs, n_6 for the first 100 μs, and $T_{\rm tr}$ for the first 200 μs have larger discrepancies with the data.

3. Sensitivity analysis

Sensitivity analysis of the twelve optimized collisional rate constants are performed for $n_4, n_6, n_4, T_{\rm tr}$ time-histories. The sensitivity coefficient of the $j^{\rm th}$ rate constant, k_j, for the time-history of A, denoted as $[A]$, is calculated by perturbing the corresponding rate constants by a factor of 2 in both positive and negative directions.

$$S_j = \frac{[A]_{2k_j}(t) - [A]_{k_j/2}(t)}{[A]_{k_j}(t)} \frac{k_j}{2k_j - 0.5k_j} \tag{15}$$

where $[A]_{2k_j}(t)$ and $[A]_{k_j/2}(t)$ are the time-history simulation of $[A]$ with rate constant k_j multiplied by 2 and 1/2.

Figure 10c shows that for electron number density n_e, the most sensitive reaction rate constants are $k^M_{Ar,c}, k^e_{Ar,c}$. This is because Ar ionization is the main pathway for electron production in the current model. Figure 10d shows that the translational temperature $T_{\rm tr}$ is insensitive to almost all the rates within the test time. This is because the translational temperature changed only a small fraction ($< 10\%$) due to Ar ionization and oxygen dissociation within the test time. Figure 10a shows that for n_4, the most sensitive reactions are $k_{14}, k^e_{14}, k^M_{Ar,c}, k^e_{Ar,c}, k^M_{4c}, k_{16}$. Figure 10b shows that for n_6, the most sensitive reactions include all the above sensitive reactions for n_4, plus k_{46}. The large sensitivity of k_{46} is corroborated by the large optimized logarithmic pre-factor of k_{46} (i.e. 6200 as shown in Table III).

IV. CONCLUSION

In this paper, we studied the collisional excitation kinetics for atomic oxygen, using the n_4, n_6, n_e, and $T_{\rm tr}$ time-histories inferred from the absorbance of two atomic oxy-

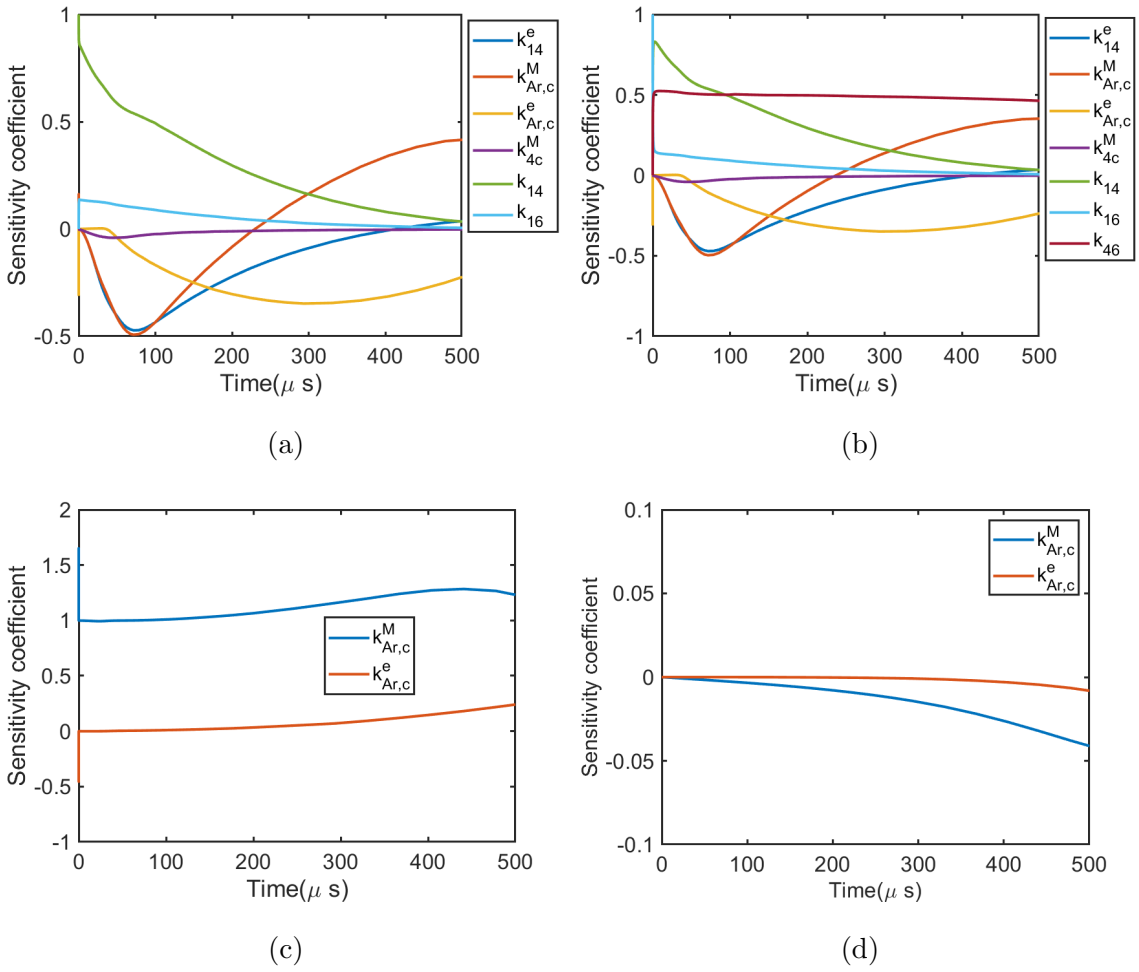

FIG. 10: Sensitivity coefficients of the most sensitive reactions for $n_4, n_6, n_e, T_{\rm tr}$ time-histories. Only a few largest sensitive rate constants are shown.

gen transitions at 777 and 926 nm. The electron number density measurements verify the faster electron production rates as hypothesized in our previous paper[17]. The n_4 and n_6 measurements show that the atomic oxygen in the energy levels 4 and 6, i.e. the O(3s ^{5}S^o) and O(3p ^{5}P$_3$) states, are in chemical non-equilibrium with atomic oxygen in the ground state, but achieve a partial equilibrium with each other within the test time of approximately 500 μs. Translational temperature inferred from the

Doppler linewidth drops within the test time because of oxygen dissociation and Ar ionization. The four measured time-histories are utilized to optimize the collisional-excitation rate constants of the simplified two-temperature collisional-radiative model using SGD algorithm. The heavy particle collisional cross-coupling rate constant between atomic oxygen in the energy levels 4 and 6, k_{46}, is found to be 6200 times larger than the nominal value adapted from the literature, to compete with the large spontaneous emission rate of A_{64} and maintain partial equilibrium between atomic oxygen in the energy levels 4 and 6. The current time-history data, diagnostic methods and collisional-radiative model may prove useful in other studies of high-enthalpy air, plasma processing or other applications involving weakly ionized oxygen, e.g. reentry flow modeling, and the data reported here may be useful to other researchers seeking to assemble kinetic models of O-atom excitation and ionization.

ACKNOWLEDGEMENT

The authors thank Prof. Mark A. Cappelli, Dr. Christopher L. Strand, Dr. Shengkai Wang, Prof. Leo Hollberg, Professor David Miller, and Dr. Jay B. Jeffries for helpful discussions. The authors also thank a reviewer for offering an interesting interpretation of the data. This work was supported by the Air Force Office of Scientific Research (AFOSR) under grant number FA9550-16-1-0291, with Dr. Ivett Leyva as the technical monitor.

---

[1] M. Panesi, T. E. Magin, and A. Bourdon. Fire II Flight Experiment Analysis by Means of a Collisional-Radiative Model. *J. Thermophys. Heat Transf.*, 23(2):236–248, 2009.

[2] A. Bultel, B. G. Chéron, A. Bourdon, O. Motapon, and I. F. Schneider. Collisional-radiative model in air for earth re-entry problems. *Phys. Plasmas*, 13:43502, 2006.

[3] X. Y. Wang, C. Yan, Y. K. Zheng, and E. L. Li. Assessment of chemical kinetic models on hypersonic flow heat transfer. *Int. J. Heat Mass Transf.*, 111:356–366, 2017.

[4] A. Bultel and J. Annaloro. Elaboration of collisional-radiative models for flows related to planetary entries into the Earth and Mars atmospheres. *Plasma Sources Sci. Technol.*, 22(2):025008, 2013.

[5] D. Olynick, W. D. Henline, L. Chambers, and G. V. Candler. Comparison of coupled radiative flow solutions with project fire II flight data. *J. Thermophys. Heat Transf.*, 9(4):586–594, 1995.

[6] G. V. Candler and R. W. MacCormack. Computation of Weakly Ionized Hypersonic Flows in Thermochemical Nonequilibrium. *J. Thermophys. Heat Transf.*, 5(3):266–273, 1991.

[7] C. Park. Review of Chemical-Kinetic Problems of Future NASA Missions, I: Earth Entries. *J. Thermophys. Heat Transf.*, 7(3):385–398, 1993.

[8] A. Lemal, C. M. Jacobs, M.Y. Perrin, C.O. Laux, P. Tran, and E. Raynaud. Air Collisional-Radiative Modeling with Heavy-Particle Impact Excitation Processes. *J. Thermophys. Heat Transf.*, 30(1):226, 2014.

[9] C. Park. *Nonequilibrium Hypersonic Aerothermodynamics.* Wiley-Interscience, New York, feb 1990.

[10] C.O. Laux. *Optical diagnostics and radiative emission of air plasmas.* PhD thesis, Stanford University, 1999.

[11] T. G. Owano. Nonequilibrium behavior in a flowing, atmospheric pressure plasma. *PhD Thesis*, 1991.

[12] C. O. Johnston, B. R. Hollis, and K. Sutton. Non-Boltzmann Modeling for Air Shock-Layer Radiation at Lunar-Return Conditions. *J. Spacecr. Rockets*, 45(5):879, 2008.

[13] Francesco Bonelli, Michele Tuttafesta, Gianpiero Colonna, Luigi Cutrone, and Giuseppe Pascazio. An MPI-CUDA approach for hypersonic flows with detailed state-to-state air kinetics using a GPU cluster. *Comput. Phys. Commun.*, 219:178–195,

2017.

[14] G. Colonna, F. Bonelli, and G. Pascazio. Impact of fundamental molecular kinetics on macroscopic properties of high-enthalpy flows: The case of hypersonic atmospheric entry. *Phys. Rev. Fluids*, 4(3):1–19, 2019.

[15] M. Nations, S. K. Wang, C. S. Goldenstein, D. F. Davidson, and R. K Hanson. Kinetics of Excited Oxygen Formation in Shock-Heated O2-Ar Mixtures. *J. Phys. Chem. A*, 120(42):8234–8243, 2016.

[16] S. M. Jo, O. J. Kwon, and J. G. Kim. Electronic-state-resolved analysis of high-enthalpy air plasma flows. *Phys. Rev. E*, 100(3):1–17, 2019.

[17] Y. Li, S. K. Wang, C. L. Strand, and R. K. Hanson. Two-temperature Collisional-radiative Modeling of Partially Ionized O2-Ar Mixtures over 8000-10,000 K behind Reflected Shock Waves. *J. Phys. Chem. A*, 124(19):3687–3697, 2020.

[18] Y. Li, S. K. Wang, S. Christopher, and R.K. Hanson. Development of a Stark Shift Measurement Technique using Excited State Oxygen Atoms to Determine Electron Number Density in Shock Heated O2/ Ar above 10,000 K. *Plasma Sources Sci. Technal.*

[19] C. Laux. Optical diagnostics of atmospheric pressure discharges. *Plasma Sources Sci. Technol.*, 12:125–138, 2003.

[20] R. Hanson, R. Spearrin, and C. Goldenstein. *Spectroscopy and optical diagnostics for gases*. Springer International Publishing, Switzerland, 2016.

[21] W.L. Wiese in. Plasma Diagnostic Techniques, Huddlestone, R. Stanley, L. Academic Press, New York, 1965.

[22] D. S. Baer, H. A. Chang, and R. K. Hanson. Fluorescence diagnostics for atmospheric-pressure plasmas using semiconductor lasers. *J. Opt. Soc. Am. B*, 9(11):1968–1978, 1992.

[23] H. Griem. *Spectral line broadening by plasmas*. Elsevier, 2012.

[24] Z. K. Hong, G. A. Pang, S. S. Vasu, D. F. Davidson, and R. K. Hanson. The use of driver inserts to reduce non-ideal pressure variations behind reflected shock waves.

Shock Waves, 19(2):113–123, 2009.

[25] A. Goly and S. Weniger. Widths and shifts of some plasma-broadened oxygen and carbon multiplets. *J. Quant. Spectrosc. Radiat. Transf.*, 38(3):225–230, 1987.

[26] J. W. Streicher, A. Krish, R. K. Hanson, K. M. Hanquist, R. S. Chaudhry, and I. D. Boyd. Shock-tube measurements of coupled vibration-dissociation time-histories and rate parameters in oxygen and argon mixtures from 5000 K to 10 000 K. *Phys. Fluids*, 32(7):0–21, 2020.

[27] O. Zatsarinny and S. S. Tayal. Electron collisional excitation rates for OI using the B-spline R-matrix approach. *Astron. Astrophys. Suppl. Ser*, 148:575–582, 2003.

[28] M. I. Hoffert and H. Lien. Quasi-One-Dimensional, Nonequilibrium Gas Dynamics of Partially Ionized Two-Temperature Argon. *Cit. Phys. Fluids*, 10:1769, 1967.

[29] A. J. Kelly. Atom-atom lonization cross sections of the noble gases-argon, krypton, and xenon. *J. Chem. Phys.*, 45(5):1723–1732, 1966.

[30] H. W. Drawin and F. Emard. Atom-atom excitation and ionization in shock waves of the noble gases. *Phys. Lett. A*, 43(4):333–335, 1973.

[31] A. Kramida, Yu. Ralchenko, J. Reader, and The NIST ASD Team (2018). NIST Atomic Spectra Database (ver. 5.6.1), [Online]. Available: http://physics.nist.gov/, 2019.

[32] J. Vlcek. A collisional-radiative model applicable to argon discharges over a wide range of conditions. I. Formulation and basic data. *J. Phys. D Appl. Phys. J. Phys. D Appl. Phys*, 22:623–631, 1989.

[33] A. Bultel, B. Van Ootegem, A. Bourdon, and P. Vervisch. Influence of Ar2+ in an argon collisional-radiative model. *Phys. Rev. E*, 65(4):046406, 2002.

[34] T. Holstein. Imprisonment of Resonance Radiation in Gases. II. *Phys. Rev. Lett.*, 83(6):1159–1168, 1951.

[35] M. G. Kapper and J. L. Cambier. Ionizing shocks in argon. Part I: Collisional-radiative model and steady-state structure. *J. Appl. Phys.*, 109(11):113308, 2011.

[36] B. J. McBride, M. J. Zehe, and S. Gordon. NASA Glenn coeefficients for calculating thermodynamic properties of individual species. (September), 2002.

[37] P. J. Dagdigian, B. E. Forch, and A. W. Miziolek. Collisional transfer between and quenching of the 3p 3P and 5P states of the oxygen atom. *Chem. Phys. Lett.*, 148(4):299–308, 1988.

Appendix A: Time-histories measurements

The absolute values of the time-histories for the n_4, n_6, n_e, and $T_{\rm tr}$ are shown in Figure 11.

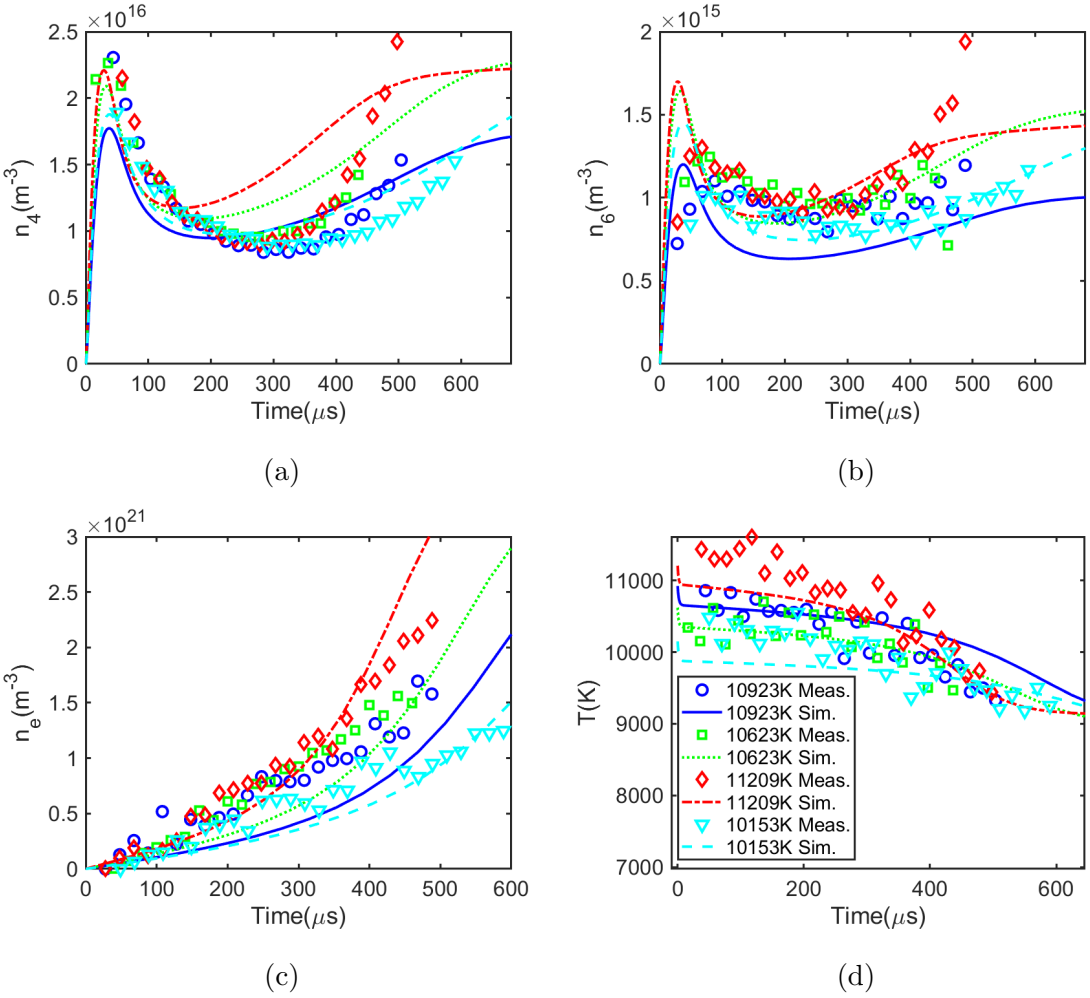

FIG. 11: Absolute values of (a)n_4 (b)n_6 (c)n_e (d)temperature from 10,100-11,200 K.Symbols: measurements. Lines: simulations using optimized models with rate constants in Table III.